Viability of video imaging spectro-radiometry (VISR) for quantifying flare combustion efficiency

Journal:	*Journal of the Air & Waste Management Association*
Manuscript ID	Draft
Manuscript Type:	Technical Paper—Air Pollution
Date Submitted by the Author:	n/a
Complete List of Authors:	Kaveh, Alireza; University of Waterloo, Mechanical and Mechatronics Engineering Spinti, Jennifer; University of Utah, ICSE Lapeyre, Paule; University of Waterloo, Mechanical and Mechatronics Engineering Bonarens, Matthias; Technical University of Darmstadt, Department of Mechanical Engineering, Reactive Flows, and Diagnostics Daun, Kyle J; University of Waterloo, Mechanical and Mechatronics Engineering
Keywords:	Flares, combustion efficiency, Remote Sensing, verification and validation, radiometric measurements
Abstract:	Video imaging spectro-radiometry (VISR) has been proposed as a means to quantify the combustion efficiency (CE) of flares. This work presents a numerical assessment of VISR using computational fluid dynamics simulations of a steam-assisted industrial flare, with a focus on three aspects: how approximations in the radiometric model impact the local "pixel-wise" CE, the validity of the approach for computing flare global CE using inferred local CE values, and the ability and limitations of VISR instrument to capture fuel that may be aerodynamically stripped from the combustion zone under crosswind conditions. The present analysis is conducted using simulated images generated over bands aligned with key absorption features of three key products of flare combustion: CO2 (4.2–4.4 μm), CO (4.5–4.9 μm), and CH4 (3.2–3.4 μm). The results show that the simplified VISR approach can predict local CE accurately; but the model used to convert these values into a flare global CE is flawed and potentially leads to large biases. Finally, since the technique relies on mid-infrared imaging, it is likely incapable of quantifying unburned (cold) methane that may be stripped from the combustion zone due to the presence of a high crosswind over the flare stack, leading to a significant overestimation of the actual flare performance.

Implications Statement

A technique called "Video imaging spectro-radiometry" (VISR) has been developed for quantifying the combustion efficiency of flares based on spectrally resolved imaging. In the original version of this technique, a multispectral camera measures emissions over spectral bands aligned with key absorption features of CO_2, CO, and the C-H stretch absorption band of alkanes. A local combustion efficiency map is defined from the ratio of the broadband pixel intensities, which is then converted into an overall combustion efficiency through pixel-averaging.

While this technique has been validated through extractive sampling studies, in this work we analyze simulated measurements using a CFD simulated steam-assisted flare. In this context the CFD data serves as a ground truth. The results call into question the veracity of the instrument model used to convert the local CE estimates into a global CE for the flare, as well as the ability of this technique to capture cold methane that may be diverted from the combustion zone through aerodynamic stripping. These findings have important implications for emerging technology-based emission regulations, as well as the development of new remote sensing technologies for measuring flare performance.

Viability of video imaging spectro-radiometry (VISR) for quantifying flare combustion efficiency

A. Kaveh[1], J. C. Spinti[2], P. Lapeyre[1], M. Bonarens[3], and K. J. Daun[1,*]

[1]*Department of Mechanical and Mechatronics Engineering, University of Waterloo, 200 University Ave W, Waterloo, ON, Canada, N2L 3G1*

[2]*Department of Chemical Engineering, University of Utah, Salt Lake City, UT, United States of America, 84112*

[3]*Department of Mechanical Engineering, Reactive Flows, and Diagnostics, Technical University of Darmstadt, Darmstadt, Germany, 64287*

* Corresponding author: kjdaun@uwaterloo.ca

ABSTRACT

Video imaging spectro-radiometry (VISR) has been proposed as a means to quantify the combustion efficiency (CE) of flares. This work presents a numerical assessment of VISR using computational fluid dynamics simulations of a steam-assisted industrial flare, with a focus on three aspects: how approximations in the radiometric model impact the local "pixel-wise" CE, the validity of the approach for computing flare global CE using inferred local CE values, and the ability and limitations of VISR instrument to capture fuel that may be aerodynamically stripped from the combustion zone under crosswind conditions. The present analysis is conducted using simulated images generated over bands aligned with key absorption features of three key products of flare combustion: CO_2 (4.2–4.4 μm), CO (4.5–4.9 μm), and CH_4 (3.2–3.4 μm). The results show that the simplified VISR approach can predict local CE accurately; but the model used to convert these values into a flare global CE is flawed and potentially leads to large biases. Finally, since the technique relies on mid-infrared imaging, it is likely incapable of quantifying unburned (cold) methane that may be stripped from the combustion zone due to the presence of a high crosswind over the flare stack, leading to a significant overestimation of the actual flare performance.

1. INTRODUCTION

The oil and gas industry relies on flaring to transform unwanted hydrocarbon (HC) gases like methane (CH_4) into species having significantly lower global warming potentials, chiefly carbon dioxide (CO_2) and water vapor (H_2O) [1]. In downstream petrochemical operations, flaring is also motivated by the direct and indirect health impacts of byproducts like highly reactive volatile organic compounds (HRVOCs) that would otherwise be released directly into the environment. Flaring effectiveness is often characterized by combustion efficiency (CE), generally defined as the fraction of carbon mass in flared gas that is converted into CO_2. The destruction removal efficiency (DRE) is a similar metric which targets a specific compound of the flared gas, e.g., the fraction of CH_4 that is converted to CO_2.

Flaring is often assumed to occur with an average CE of 98% [2–4]; however, recent studies suggest that this figure may be significantly lower due to factors including strong crosswinds [5,6], steam and air assistance [7–9], and the low heating value of the fuel [5,6,9–11]. Increasing awareness of the detrimental health and environmental consequences of unburned and partially-pyrolyzed flared gas, coupled with increasingly strict methane emission regulations [12,13], presents an urgent need for robust diagnostics instrumentation capable of determining accurate estimates of flare CE.

Infrared remote sensing methods over the mid-wavelength infrared (MWIR) and long-wavelength infrared (LWIR) spectra are good candidates for this purpose since they do not require direct access to the flare plume, and, in some cases, may provide a CE estimate without independent knowledge of the flare gas constituents and flow rates. One of the earliest remote sensing approaches is passive Fourier transform infrared (PFTIR) spectroscopy [14–17], which uses an open-path FTIR spectrometer to obtain gas species concentrations along a single line-of-sight (LOS) through the plume; the measured spectra are then converted into a local CE estimate assuming a homogeneous plume. These instruments operate at a spectral resolution of approximately 0.5 cm^{-1} [18], sufficient to resolve key absorption lines of the various plume species. Consequently, the inferred CE depends strongly on the chosen LOS, and a common strategy is to aim the PFTIR at a point one flame length downwind of the visible flame tip [18]. A major drawback of this approach is that it does not account for the dynamic motion of the flare plume, nor the possibility of a heterogeneous plume composition.

In recent years, commercial multispectral and hyperspectral imagers enable spectrally and temporally resolved intensity measurements across the entire flare plume. Post-processing of these spectral measurements provides a means to infer the column density of carbon-containing species along the LOS aligned to each pixel in the image, ideally capturing the species distribution through the entire plume region. The "local" pixel-wise CE can then be used to compute an overall flare CE or species-specific DREs. Candidate devices in this class of instruments include imaging Fourier transform spectrometers (IFTSs) [19–21], which are based on interferometry, as well as light-field (plenoptic) [22] and line-scan [23] cameras. While IFTSs provide a high degree of spatial and spectral resolution, they also have several key drawbacks. First, even though the IFTS uses a high frame rate camera (~1 kHz) to capture the interferogram images, each interferogram contains thousands of plume images and thus requires tens of seconds to minutes to acquire depending on spectral resolution. Furthermore, turbulent fluctuations in the flare plume contaminate the interference patterns in the interferogram data cube, leading to scene-change artifacts (SCAs) that contaminate the transformed radiance spectra [24,25]. In the case of a stationary plume, these artifacts may be mitigated by median-filtering multiple interferograms [25], which further lowers the temporal resolution of the hyperspectral images.

Line-scan and light-field imagers are considerably faster than IFTSs, although they have significantly lower spectral resolution. In 2012, Zeng et al. proposed using a four-channel light-field imager to quantify flare CE [22]. The light-field imager would use a microlens array to project four copies of the scene through corresponding broadband filters located adjacent to a camera sensor subdivided into quadrants. The filters would be positioned behind the cold shield of the camera to minimize blackbody emission from the opaque regions of the filters, which would otherwise dominate the signal. Zeng et al. proposed filter windows aligned with key vibrational-rotational (VR) bands of CO_2 (4.2–4.4 μm), CH_4 (4.5–4.9 μm), and CO (3.2–3.4 μm), with an additional band aligned with a transparent window corresponding to the atmospheric background radiance [22]. Through several assumptions and simplifications, the broadband intensities would be correlated to the corresponding species column density along the LOS of each pixel inside the plume. The column densities would then be converted into a local CE for each pixel. Finally, and crucially, the flare CE would be taken as the mean local CE of the detectable pixels located outside the flame envelope that separates the region where combustion is occurring and the one that contains the fully combusted plume species.

Zeng et al. [23] implemented this approach using a commercial line-scan camera (Surface Optics Corporation SOC 750C) that generates a data cube of 42 uniformly spaced spectral channels between 2 to 5 μm at a rate of 11 data cubes (256 pixels × 240 pixels × 42 bins) per second. They assessed the performance of this approach on steam- and air-assisted flares burning various mixtures of propane, propylene, and natural gas. A comparison between the VISR-inferred flare CEs and values found from extractive sampling, using an exhaust hood located on top of the flare plume, showed good quantitative agreement (Fig. 1). From these results, the manufacturer of this technology has claimed an "accuracy within 1%" [26] based on the absolute difference between the CE values under efficient flare operating conditions (CE >~ 97%). The VISR technology has been commercialized as the FlareGuardian^{TM} system, which replaced the line-scan imager with a light-field camera having a similar number of channels but operating within a narrower spectral range of 3–5 μm and with band spacings optimized to capture key absorption features of the species-of-interest.

Despite the promising results described in previous field assessments [23], questions about the accuracy and physical relevance of the VISR approach remain. Specifically:

1. How do the simplifications and assumptions made to derive the radiometric measurement model (i.e., a homogeneous plume composition along each LOS and the optically thin assumption) impact the local CE estimates?
2. Is the approach used to convert the local (pixel-wise) CE estimates into the global CE estimate unbiased, and is it physically meaningful?
3. Can the VISR technique quantify cold (unburned) fugitive hydrocarbons in the case of crosswind-induced aerodynamic fuel stripping?

It is difficult to answer these questions through physical experimentation due to the inherent uncertainty associated with extractive sampling, in particular, the fact that it only provides the flare plume composition at one location, usually directly behind the visible flame. Moreover, these measurements cannot be used to isolate errors originating from the simplifications made to the radiometric model, the flare CE inference method by averaging the local CE, and the limited hardware detection capabilities.

Instead, in this work we assess the performance of VISR using temperature and concentration fields developed from CFD simulations of steam-assisted flares in crosswinds. For simplicity, we

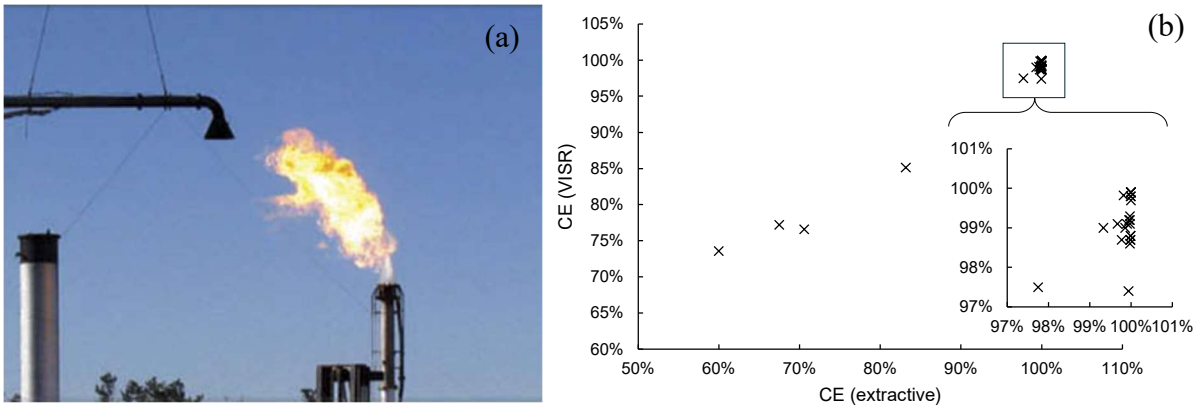

Fig. 1: (a) Image showing extractive sampling from a flare plume [23]; (b) comparison between global CE values estimated using VISR with those found through extractive sampling [23].

consider the original four-channel configuration proposed in the original VISR patent [22]. Our results suggest that the VISR approach, as defined in Refs. [22] and [23], can yield accurate local CE estimates. However, the averaging technique used to estimate global CE does not reflect the underlying transport phenomena in the flare plume and may result in large biases compared to ground-truth CE obtained from the CFD. Additionally, due to the limited dynamic range of the sensor, a significant portion of stripped flare gas is likely to remain undetected. This could lead to a significant overestimation of flare CE, particularly under high crosswind conditions.

2. FLARE COMBUSTION EFFICIENCY

Flare combustion efficiency is generally defined as the fraction of carbon in the fuel stream supplied to the flare that is ultimately converted into CO_2. In many scenarios, the fuel composition and flow rate may not be known, in which case the carbon flow rate entering the flare may be inferred through a mass balance of carbon-containing species within the plume region:

$$\mathrm{CE} = \frac{\dot{m}_{\mathrm{C,CO_2}}}{\dot{m}_{\mathrm{C,fuel}}} \approx \frac{\dot{m}_{\mathrm{C,CO_2}}}{\dot{m}_{\mathrm{C,CO_2}} + \dot{m}_{\mathrm{C,HC}} + \dot{m}_{\mathrm{C,CO}} + \cdots} \tag{1}$$

where "HC" refers to the unburned hydrocarbon components of the injected fuel stream to the flare stack. Carbon mass flow rates are found by multiplying the total mass flow rates by the molecular mass fraction of carbon-containing species. In principle the denominator in Eq. (1) includes all carbon-containing by-products in the flare plume, although it is mainly dominated by CO_2 and the unburned hydrocarbon components of the fuel stream [27].

In principle, the mass flow rates in Eq. (1) can be obtained by integrating mass fluxes along a control volume that envelopes the plume. The mass fluxes, in turn, are the product of volumetric species concentrations located at the edge of the control surface and a corresponding velocity, normal to the control surface. When analyzing the results of a CFD simulation, this may be done approximately using a quadrature scheme.

In the context of imaging techniques, it is often convenient to derive a local (pixel-wise) combustion efficiency based on the ratio of the column number densities of carbon-containing species, weighted by the number of carbon atoms per molecule, $n_{C,k}$. More precisely, for the jth pixel the local CE is expressed as

$$\mathrm{CE}_j = \frac{\sigma_{\mathrm{CO}_2,j}}{\sum_k n_{\mathrm{C},k}\sigma_{k,j}} \tag{2}$$

where $\sigma_{k,j}$ is the column number density of the kth species (molecules/m^2). This parameter is obtained by integrating the local number density, $N_{k,j}$, along the jth pixel LOS

$$\sigma_{k,j} = \int_0^L N_{k,j}(s)\,ds = \int_0^L \frac{\chi_{k,j}(s)p}{k_{\mathrm{B}}T_j(s)}\,ds \tag{3}$$

where k_{B} is Boltzmann's constant, $\chi_{k,j}$ (s) and T_j (s) are the mole fraction and temperature profiles at a location s along the jth LOS, and L is the plume width (into the image plane). The atmospheric pressure, p, is taken to be uniform through the plume.

The connection between the "local" CE, Eq. (2), and the "global" CE, Eq. (1), is not straightforward. Zeng et al. [22,23] suggest that the overall flare CE could be estimated by the mean local CE of pixels located within an envelope surrounding the combustion zone, rationalizing that these pixels are likely to contain gaseous by-products of the complete combustion process, and therefore taking the "average" of the local CEs represents the average carbon conversion performance of the flare. They define the inner envelope surface as the region in the vicinity of the flame zone where the CE increases abruptly, indicating the completion of the combustion reaction, while the outer surface corresponds to areas with almost undetectable broadband intensity. We will assess the veracity of this treatment later in the paper.

3. MEASUREMENT MODEL

The local CE in Eq. (2) is related to the set of broadband spectral intensities measured for each pixel through a measurement model composed of a radiometric sub-model and an instrument sub-model.

3.1.Radiative transfer equation

Figure 2 shows a schematic of the radiometric measurement. The influence of absorption and emission of the atmospheric layer between the flare and the camera aperture is excluded from the present analysis, but it could be accounted for by examining a "background pixel" at a similar distance from the camera as the flare plume, e.g. the flare stack, in combination with the intensity measured by the "transparent" channel. Since molecular gas scattering at mid-infrared wavelengths is negligible over the pathlengths considered here, the spectral intensity incident on the camera aperture at wavenumber η is given by

$$I_{\eta,L} = I_{\eta,\mathrm{bg}} \exp\left[-\int_0^L \kappa_{\eta,\mathrm{mix}}(s)\,ds\right] + \int_0^L \kappa_{\eta,\mathrm{mix}}(s)\, I_{\eta\mathrm{b}}\left[T(s)\right] \exp\left[-\int_s^L \kappa_{\eta,\mathrm{mix}}(s')\,ds'\right] ds \qquad (4)$$

where $I_{\eta,\mathrm{bg}}$ is the background irradiation, $I_{\eta,\mathrm{b}}$ is the spectral blackbody intensity, L is the plume thickness, $\kappa_{\eta,\mathrm{mix}}$ is the absorption coefficient of the gas mixture and $T(s)$ is the plume temperature at a parametric location s along the pixel LOS. The absorption coefficient of the gas mixture at location s along the pixel LOS is the sum of the absorption coefficients of all participating species at the same location

$$\kappa_{\eta,\mathrm{mix}}(s) = \sum_k C_{\eta,\mathrm{abs},k}\left[T(s)\right] N_k(s) \qquad (5)$$

where N_k and $C_{\eta,\mathrm{abs},k}$ are the local number density, derived along the corresponding pixel LOS, and the molecular spectral absorption cross-section of the kth component inside the plume, respectively. The spectral absorption cross-section can be computed as a function of the local temperature using the HITRAN database [28].

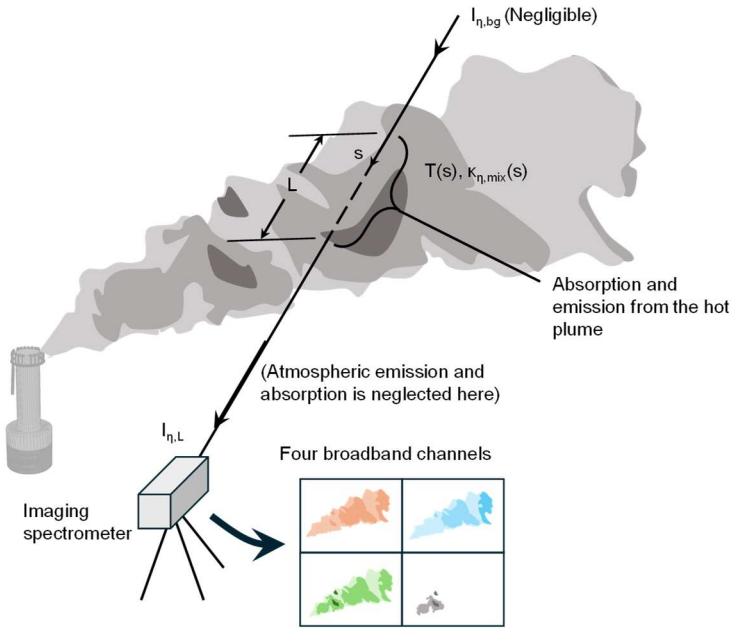

Fig. 2: Schematic of a four-channel VISR radiometric measurement.

The incident intensity entering the camera aperture along each pixel LOS is spectrally integrated, e.g., by capturing the scene through a series of spectral broadband filters and then imaging it onto an IR sensor. Assuming idealized "top hat" filters that are perfectly transparent over the corresponding detection spectrum, $\Delta\eta_k$, the signal of the kth channel for the jth pixel is given by

$$S_{k,j}^{\text{exact}} = C_k \int_{\Delta\eta_k} I_{\eta,L}\, \mathrm{d}\eta \tag{6}$$

where C_k is a calibration constant that accounts for the detector sensitivity, pixel spatial resolution, integration time, and pixel solid angle, and I_η is the spectral intensity, obtained by applying Eq. (4) to the jth pixel LOS. Calibration constants are assumed to be perfectly known and taken as unity.

Following Zeng et al. [22], the selected spectral channels are broadly aligned with spectral absorption features of CH_4 (Channel 1, 3.2–3.4 μm), CO_2 (Channel 2, 4.2–4.4 μm), and CO (Channel 3, 4.5–4.9 μm), while the fourth transparent channel is excluded from the analysis. Figure 3 shows a simulated emission spectrum made using the CFD-simulated flare plume described in the next section and the alignment of the bandpass filters. The VISR method, as defined by Zeng et al. [22], assumes that the flare fuel is composed entirely of CH_4, which may be reasonable in the case of upstream flaring but is less certain in other flaring scenarios, such as petrochemical

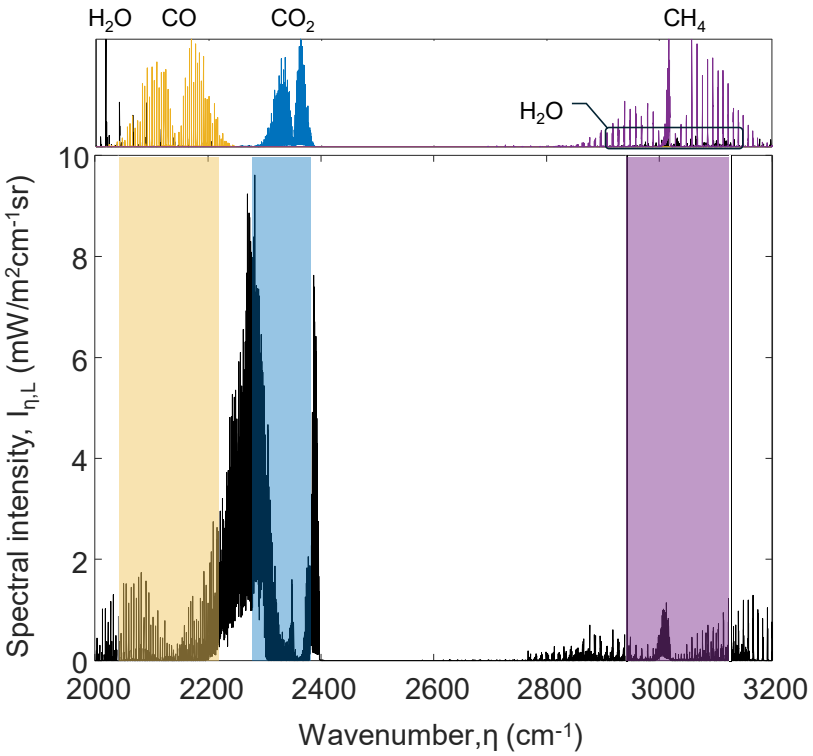

Fig. 3: Incident intensity spectrum along the line-of-sight of a sample pixel, along with the filter windows used to generate the measurement channels. Spectral lines (normalized for each species) are plotted at the top.

refining. Figure 3 also reveals very few H_2O lines over the detection spectrum, which is a key attribute of MWIR imaging. While one would expect a stronger HC signal in the LWIR, the presence of overlapping H_2O and HC lines would be far more challenging to detangle, particularly when using an instrument having limited spectral resolution.

3.2.VISR model implementation

The radiometric model defined by Eqs. (4)-(6) is too computationally demanding and complex to be inverted directly for the unknown temperature and species column number densities needed to compute the local CE, particularly if the goal is to provide near real-time feedback on flare performance. Instead, Zeng et al. [22] developed an explicit formula for the local CE by assuming: (i) a uniform temperature profile along each pixel LOS (a well-mixed plume); (ii) an optically thin plume medium (i.e., no self-absorption); (iii) the *k*th channel intensity only corresponds to contributions from the spectral absorption features of the *k*th carbon-containing species; and (iv) negligible background intensity. Following these assumptions, Eq. (4) may be rearranged into

$$I_\eta \approx I_{\eta,b}(T)\ \tau_{\eta,L}(T) \tag{7}$$

where the optical thickness, $\tau_{\eta,L}$, is defined according to the Beer-Lambert law,

$$\tau_{\eta,L}(T) = \int_0^L \kappa_{\eta,k}(s)\,ds = \int_0^L \alpha_{\eta,k}\left[T(s)\right] N_k(s)\,ds = \alpha_{\eta,k}(T)\,\sigma_k \tag{8}$$

Substituting Eq. (8) into Eq. (7) yields the final expression for the VISR spectral intensity

$$I_\eta \approx I_{\eta,b}(T)\ \alpha_{\eta,k}(T)\ \sigma_k \tag{9}$$

By approximating the blackbody intensity as spectrally uniform over each filter window, the broadband pixel intensity (pixel brightness) for the *k*th channel of the *j*th pixel is expressed by

$$S_{k,j} \approx C_k\,\Delta\eta_k \left\langle I_{\eta_k,\mathrm{b}}(T_j)\ \alpha_{\eta,k}(T_j)\right\rangle_{\eta_k} \sigma_{k,j} \tag{10}$$

Rearranging for the species-of-interest column number densities and substituting the result into Eq. (2) yields

$$\mathrm{CE}_j \approx \frac{S_{\mathrm{CO}_2,j} \Big/ \left[C_{\mathrm{CO}_2}\Delta\eta_{\mathrm{CO}_2} \left\langle I_{\eta_{\mathrm{CO}_2},\mathrm{b}}(T_j)\ \alpha_{\eta,\mathrm{CO}_2}(T)\right\rangle_{\eta_{\mathrm{CO}_2}} \Big/ n_{\mathrm{C,CO}_2}\right]}{\sum_{k=1}^{3} S_{\mathrm{k},j} \Big/ \left[C_k\Delta\eta_k \left\langle I_{\eta_k,\mathrm{b}}(T_j)\ \alpha_{\eta,k}(T)\right\rangle_{\eta_k} \Big/ n_{\mathrm{C},k}\right]} \tag{11}$$

The effective pixel plume temperature, T_j, influences the flare CE estimates through both the absorption line strengths in $\alpha_{\eta,k}$, and the ratio of blackbody intensities of the spectral channels.

Finally, the inferred local (pixel-wise) CE values are averaged over the VISR region of interest (ROI), having an inner surface defined by the outer boundary of the flame envelope and an outer surface limited to the region where the observed spectral signal is detectable, above the camera noise threshold (NESR). According to Zeng et al. [22,23], the inner region may also be approximated by a particular isotherm surrounding the visible flame boundary. These two surfaces define the VISR ROI, which is shown conceptually in Fig. 4. This averaging amounts to

$$\mathrm{CE}_{\mathrm{VISR}} = \frac{1}{N_{\mathrm{ROI}}}\sum_{j=1}^{N_{\mathrm{ROI}}} \mathrm{CE}_j = \frac{1}{N_{\mathrm{ROI}}}\sum_{j=1}^{N_{\mathrm{ROI}}} \left(\frac{n_{\mathrm{C,CO}_2}\sigma_{\mathrm{CO}_2,j}}{\sum_k n_{\mathrm{C},k}\sigma_{k,j}} \right) \tag{12}$$

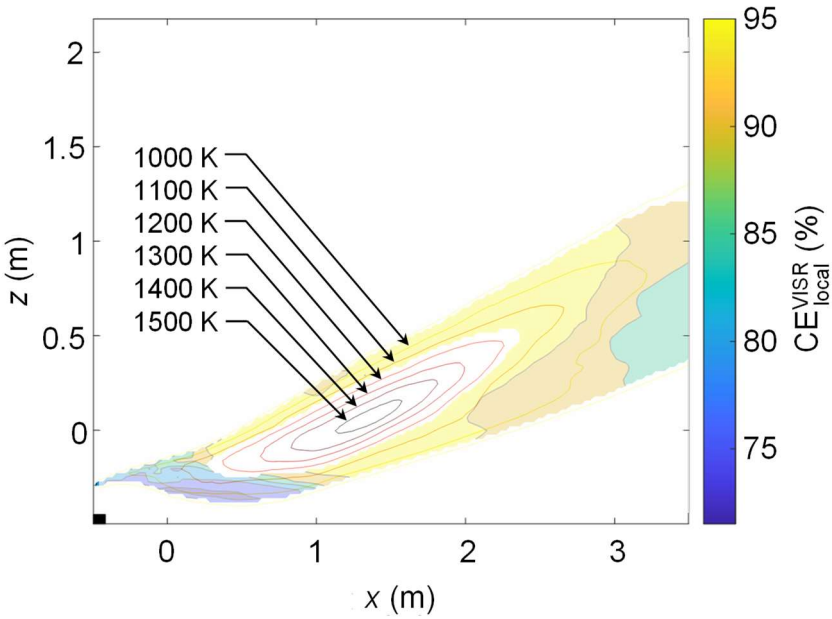

Fig. 4: Sample illustration of the VISR ROI, comprised of pixels with detected spectral signal located outside the flame envelope. Isotherms are taken along the plume centerline. The flame envelope, shown as the white region within the detectable VISR ROI, can be approximated by an isotherm confining the visible flame, per the description provided by Zeng et al. [22,23].

4. SIMULATED VISR FLARE MEASUREMENTS

The performance of the VISR technique is assessed through simulated radiometric measurements on a steam-assisted flare operating in a crosswind using CFD-LES data. The flare stack has an outer diameter and height of 0.128 m and 0.5 m, respectively, and is terminated with a John Zink SKEC© flare tip. Injected natural gas, composed of 95% methane, 4.5% ethane, and 0.5% propane by volume, exits the flare tip with a velocity of 1.2 m/s at 298 K and reacts with a mixture of crosswind ambient air with uniform velocity. Fuel-air mixing is assisted by saturated water vapor to suppress excessive smoke generation. Table 1 summarizes the crosswind and steam-assist rates considered in this analysis.

The governing transport equations are solved using the Uintah-Arches LES solver [29], which incorporates a two-step modelling strategy for the turbulent CH_4 combustion based on the rate-controlled constrained equilibrium (RCCE) method [30,31]: a slow step utilizing the Westbrook and Dryer single-step mechanism [32] that is computed using LES-filtered quantities, and an infinitely fast step at the LES sub-grid scale that yields chemical equilibrium. The combustion model also includes the Dryer and Glassman reduced-order model [33] to account for

nonequilibrium CO oxidation kinetics. Radiative heat transfer is modelled using the Discrete Ordinates Method (DOM) with S_2 quadrature [34].

The CFD-LES cases are summarized in Table 1. Each domain is discretized into $8 \times 8 \times 8$ mm^3 cube elements. To fully capture the transient behaviour of the plume, the CFD-LES simulations were run for a minimum of 10 s of simulation time with timesteps on the order of 10^{-5} s.

Table 1: CFD-LES simulation case studies.

Case	Crosswind uniform velocity at 298 K (m/s)	Assist steam mass flow rate at 373 K (g/s)	Total number of cubic elements	CFD-LES domain size (m × m × m)
1	2.2352	16.38	37,687,500	4.0 × 1.8 × 2.68
2	4.2448	10.694	23,500,400	3.92 × 1.76 × 1.75
3	5.0232	70.539	11,704,000	3.04 × 1.12 × 1.76
4	6.174	160.8	7,087,500	2.0 × 1.08 × 1.68

The simulated temperature and species concentration profiles are substituted into Eq. (4) to generate spectral intensity, which is then transformed into vectors of the exact broadband data, $\mathbf{b}^{\text{exact}} = [S_1^{\text{exact}}, S_2^{\text{exact}}, S_3^{\text{exact}}]$ via Eq. (6). Figure 5 shows simulated time-averaged broadband intensity images of the three VISR-specified spectral channels corresponding to Case 2.

Finally, the simulated broadband intensities are contaminated with artificial white noise sampled from an unbiased Gaussian distribution derived from a noise equivalent temperature difference (NETD) of 0.035 (m·K), typical of the SOC750 used by Zeng et al. [23] for VISR

$$\mathbf{b}^{\text{meas}} = \mathbf{b}^{\text{exact}} + \boldsymbol{\delta}\mathbf{b}^{\text{noise}}, \quad \boldsymbol{\delta}\mathbf{b}^{\text{noise}} \sim \mathcal{N}\left(0, \boldsymbol{\Gamma}_{\text{NETD}}\right) \tag{13}$$

Crucially, the NETD defines the outer detection envelope and limits the camera's ability to resolve pixels containing unheated fuel that has been aerodynamically stripped from the combustion zone. In their experimental analysis, Zeng et al. [23] temporally averaged 325 data cubes to reduce the number of data sets that would need to be processed analytically, although this also improved the signal-to-noise (S/N) ratio. We explore this effect by averaging temporally resolved synthetic images over approximately five seconds, resulting in an extended region of detected intensity across all the VISR spectral bins.

A noise threshold is introduced to the simulated broadband images, based on the overall net equivalent spectral radiance (NESR) value. The implemented noise threshold filters out the pixels with a low S/N ratio, depicted by the white region in Fig. 6. This effect is most pronounced for the CH_4 and CO channels at high and low flare CE, respectively, since these scenarios coincide with

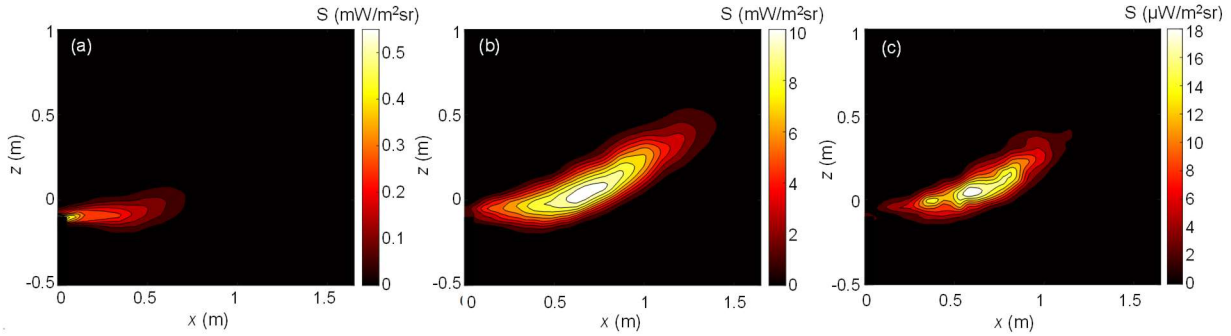

Fig. 5: Exact time-averaged broadband images of the VISR camera for Case 2, illustrated for spectral channels corresponding to: (a) CH_4 (3.2-3.4 μm), (b) CO_2 (4.2-4.4 μm), and (c) CO (4.5-4.9 μm).

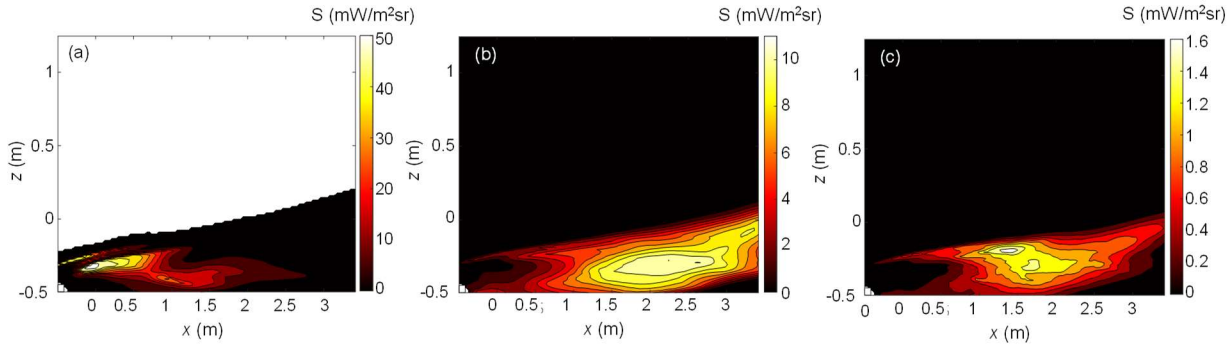

Fig. 6: Synthetic broadband images of the VISR camera for Case 2 at an arbitrary timestep, illustrated for spectral channels corresponding to: (a) CH_4 (3.2–3.4 μm), (b) CO_2 (4.2–4.4 μm), and (c) CO (4.5–4.9 μm). The white region in Fig. 6 (a) represents pixels with undetectable signals reaching over the noise threshold/ below the NESR.

the lowest abundance, temperature, and concentrations of those species in the flare plume. In principle, the finite dynamic range of the camera likely means that some pixels in the combustion zone may also be saturated, although this effect is not considered here.

Finally, while the CFD simulations have been validated against experimental measurements conducted within a wind tunnel [29], it is important to note that the veracity of the CFD measurements is not crucial to this procedure. This is because both the local and global combustion efficiencies and the radiance measured by the camera are obtained from the same CFD data that acts as a "ground truth". This is a key advantage of conducting measurements in silico, versus experimental validation procedures that can be confounded by unavoidable artifacts, including, e.g., the location of the sampler shown in Fig. 1 (a).

5. RESULTS AND DISCUSSION

5.1. Accuracy of local CE estimates

We first investigate the impact of the optically thin and uniform temperature assumptions made to transform the non-scattering RTE, Eq. (4), into local (pixel-wise) CE estimates using the VISR radiometric model, Eq. (10). Figure 7 shows sample 2D contours of the VISR-inferred and ground-truth local CE for Case 1 (see Table 1), the latter obtained by substituting LES-computed species column number densities into Eq. (3). Figure 7 also shows the relative error (RE) between these quantities for pixels within the VISR ROI at an arbitrary timestep. Figure 8 plots the relative error in the local CE as a function of the VISR-inferred estimate for all pixels and all timesteps within the VISR ROI. For pixels within the ROI, the VISR-inferred local CE values are typically within 3% of the true values, although the errors are significantly higher within the visible flame region.

A key advantage of using CFD data is the ability to distinguish the influence of the two underlying RTE simplifications on the model error. We first consider the impact of the optically thin approximation by comparing the ground-truth broadband intensities, Eq. (6), with and without the self-absorption term in the non-scattering RTE, Eq. (4). Figure 9 shows the RE associated with the optically thin approximation for pixels residing inside the ROI over all three spectral bands at an arbitrary timestep for Case 1. In contrast, the RE for pixels within the combustion zone may be as large as 10%, suggesting that this part of the image may not be modeled as optically thin.

The assumption of a uniform temperature profile along each LOS inside the plume region has a much larger impact on the accuracy of the broadband images. Figure 10 shows the temperature and species concentration profiles along the LOS of three sample pixels, identified in Fig. 7 (c), paired with the corresponding RE between the true and predicted values. The relative errors plotted in Figure 11 suggest that within the ROI, the gas plume is sufficiently well-mixed downstream of the combustion zone to produce errors of less than 2% in the broadband intensity across all channels. In regions closer to the combustion zone, where there are more pronounced gradients in temperature and species concentration, the errors approach 10% for some channels. One would expect large temperature and species concentration variations along the LOS of pixels located within the visible flame domain, which contains both combustion products and unburned reactants, resulting in significant discrepancies from the uniform distribution assumption.

Overall, however, the comparison between the VISR-inferred and CFD ground-truth local CE supports the simplifications made to the RTE, for the pixels contained within the flame envelope.

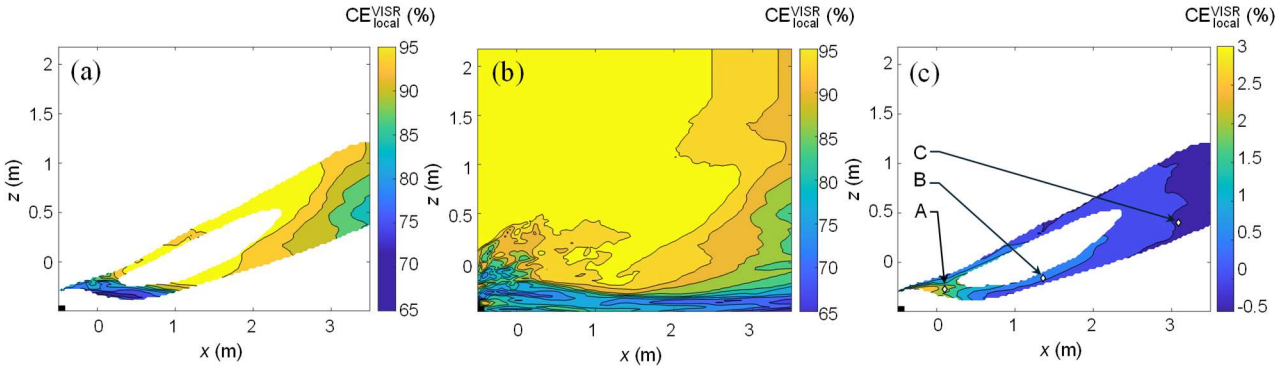

Fig. 7: Sample 2D contours of: (a) VISR-inferred local CE, (b) ground-truth local CE and (c) relative error associated with VISR-inferred local CE for Case 1 at an arbitrary timestep. Points A, B, and C correspond to profiles shown in Fig. 9.

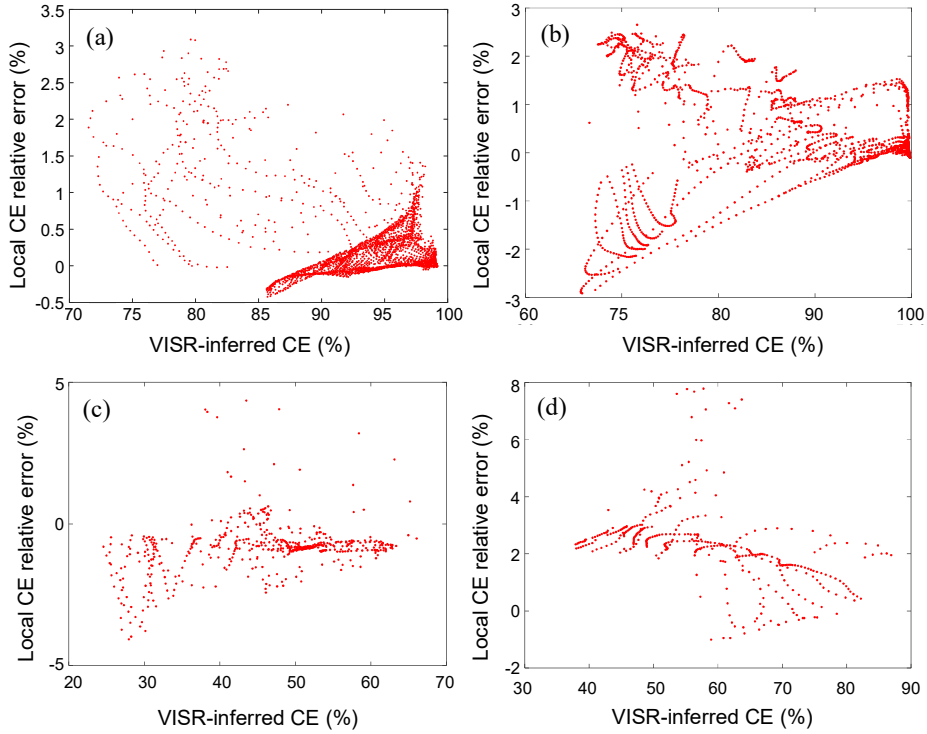

Fig. 8: Correlation between inferred local CE using the VISR technique and its corresponding relative error for the pixels located within the VISR ROI for (a) Case 1, (b) Case 2, (c) Case 3, and (d) Case 4.

5.2. Validity of the technique used to predict the global CE

Zeng et al. [22,23] propose that the global CE of a flare may be estimated by averaging the local CE of the pixels within the VISR ROI. This definition differs from Eq. (1), which is based on the total mass flow rates of the species crossing a control volume leaving the flare plume. Specifically, Eq. (1) may be written

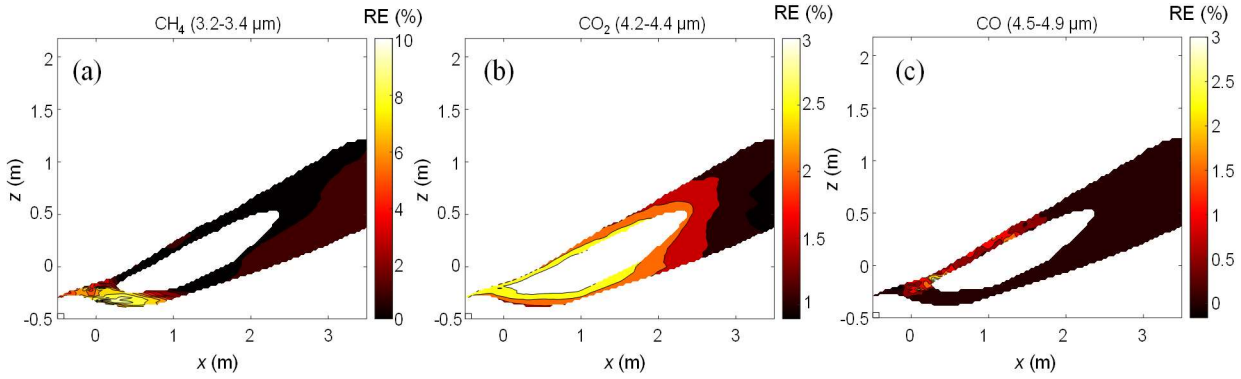

Fig. 9: Relative error in broadband intensity associated with the optically thin plume approximation, for pixels located within the VISR ROI at an arbitrary time step for Case 1.

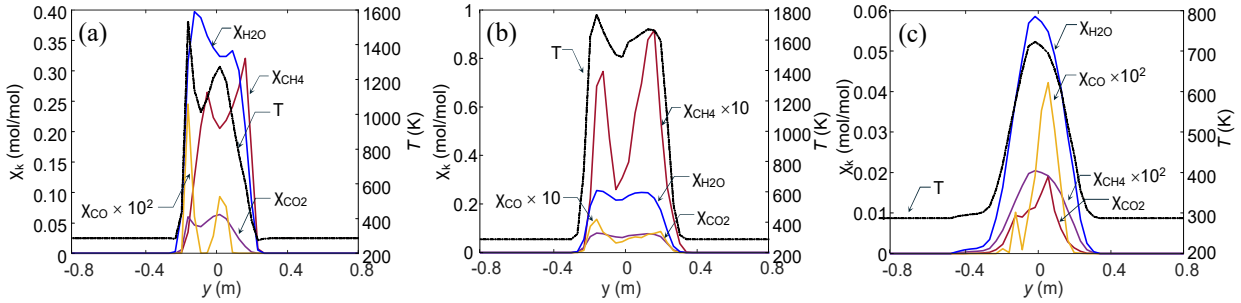

Fig. 10: Plume gas mixture temperature and carbon-containing species concentration profiles along the LOS for sample pixels (a) "A", (b) "B", and (c) "C" shown in Fig. 7. The relative differences between the true and VISR-predicted CEs are 2.2%, 0.59%, and -0.08%, respectively.

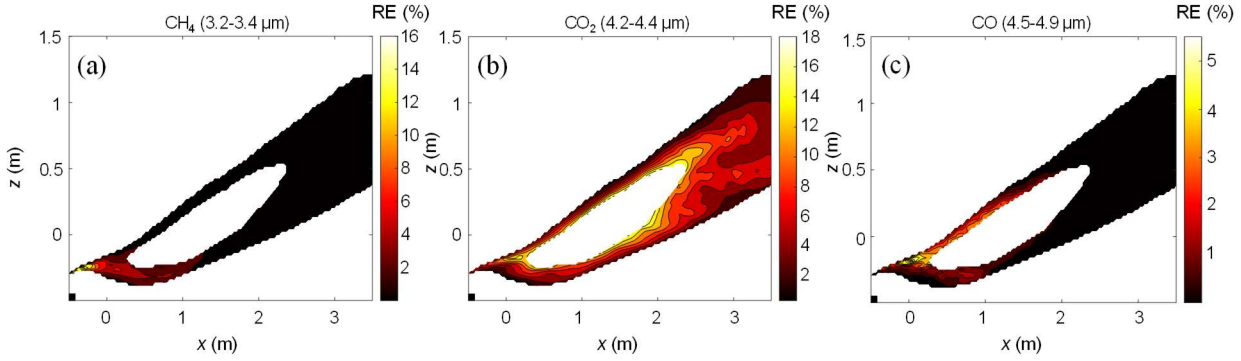

Fig. 11: Relative error in broadband intensity associated with the uniform temperature distribution assumption, for pixels located within the VISR ROI at an arbitrary time step for Case 1.

$$\mathrm{CE} = \frac{\oint_{\mathrm{CV}} \sigma_{\mathrm{C,CO2}}\, \mathbf{u}\cdot\hat{\mathbf{n}}\, ds}{\sum_k \oint_{\mathrm{CV}} n_{\mathrm{C},k}\, \sigma_{\mathrm{C},k}\, \mathbf{u}\cdot\hat{\mathbf{n}}\, ds} = \frac{\oint_{\mathrm{CV}} \sigma_{\mathrm{C,CO2}}\, \mathbf{u}\cdot\hat{\mathbf{n}}\, ds}{\oint_{\mathrm{CV}} \sum_k n_{\mathrm{C},k}\sigma_{\mathrm{C},k}\, \mathbf{u}\cdot\hat{\mathbf{n}}\, ds} \tag{14}$$

where ds is an infinitesimal length along the ROI boundary, and $\mathbf{u}$ and $\hat{\mathbf{n}}$ are the local mass-weighted velocity and unit normal vector, respectively. The summation in the denominator of Eq.

(14) may be incorporated into the integral since all species have the same projected velocity at a given plume location. The integrals in Eq. (14) may be approximated by the summation of computational cells located along the boundary,

$$\mathrm{CE} \approx \frac{\sum_{j=1}^{N} \sigma_{\mathrm{C,CO_2},j} \left(\mathbf{u}\cdot\hat{\mathbf{n}}\right)_j \Delta s_j}{\sum_{j=1}^{N}\sum_{k} n_{\mathrm{C},k}\sigma_{\mathrm{C},k,j} \left(\mathbf{u}\cdot\hat{\mathbf{n}}\right)_j \Delta s_j} \tag{15}$$

This approximation differs from Eq. (12) in two important ways: (*i*) Eq. (15) explicitly considers the advection of species into and out of the control volume, while Eq. (12) does not; and (*ii*) the summation in the denominator of Eq. (15) is applied over the entire boundary, while in Eq. (12) the carbon column number density affixed to the CO_2 of each pixel is normalized by the total carbon column number density of the corresponding pixel and not the overall value within the ROI. Coupled with the fact that the combustion products should be concentrated downwind of the combustion zone, and not upwind, the velocity terms give more weight to pixels located on the downwind surface of the control boundary, while in the VISR approach, all pixels in the ROI have equal influence on the CE estimate. As a result, pixels containing lower concentrations of combustion byproducts (either as unburned HCs, CO_2, or CO) will have an outsized influence on the average CE.

Figure 12 compares the instantaneous VISR global CE estimates found using Eq. (12) and those from the CFD "ground truth" found from Eq. (1), for the four simulation cases. In all cases, the VISR-inferred CEs differ by as much as 25% from the CFD-LES ground truth. In contrast, Zeng et al. [23] found the average difference between CE_{VISR} and the value inferred by extractive sampling to be 0.5% (absolute difference in CE, not relative error). There are two possible reasons for this disparity. First, for all but five of the 28 comparative cases considered by Zeng et al. [23], the flares were operated at CEs greater than 99%. Considering the lower CE cases alone, the difference between CE_{VISR} and the extractive sampling values is more typical of the differences observed here. Second, the inferred CE from extractive sampling is subject to its own uncertainties, as described at the beginning of this paper, and may not reflect the flare CE represented by Eq. (1)

.

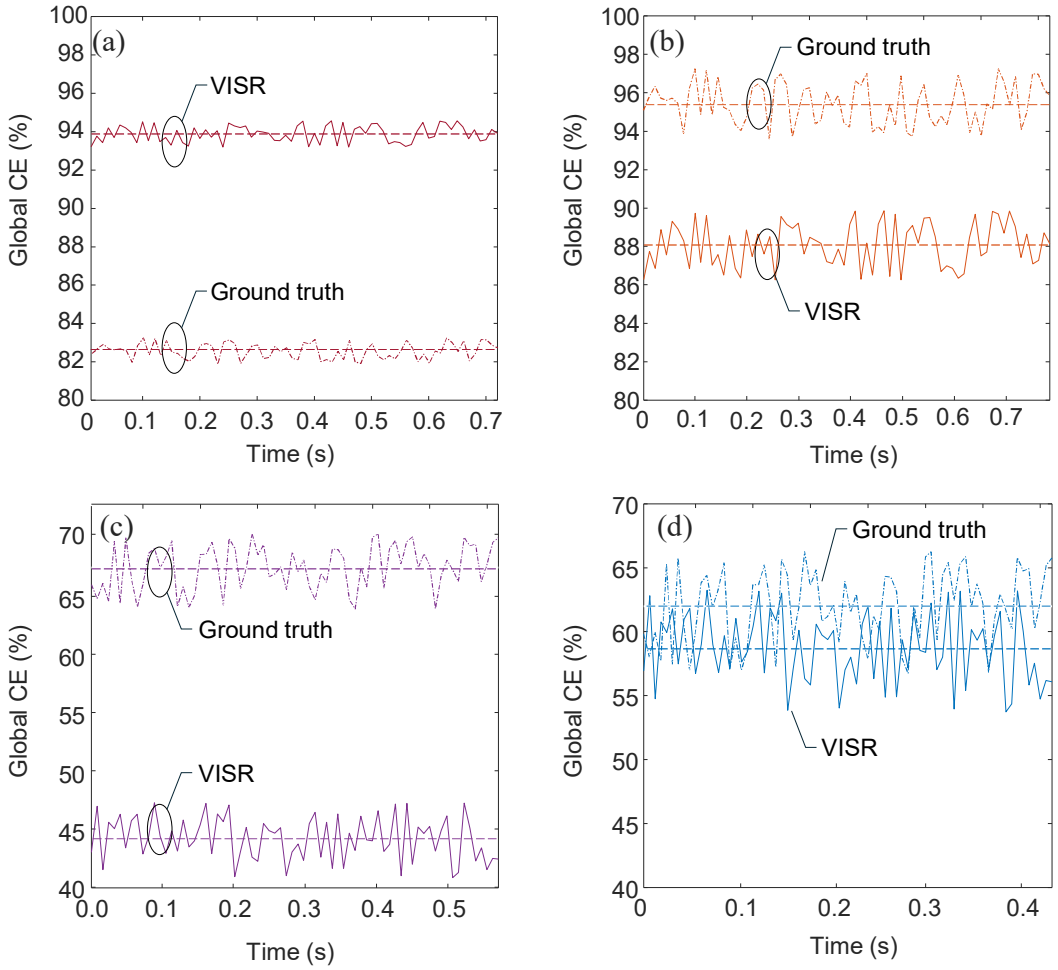

Fig. 12: Comparison between instantaneous (temporally resolved) VISR-inferred and ground truth values of global CE for 72 timesteps for (a) Case 1, (b) Case 2, (c) Case 3, and (d) Case 4. Horizontal lines indicate the corresponding time-averaged values.

5.3. Ability of the VISR technique to detect cold methane

In the case of strong crosswinds, vortices that form in the wake of the flare stack may extract localized pockets of unburned fuel from the flare tip and strip them away from the combustion zone. In contrast to the hot combustion by-products, the cold unburned CH_4 tends to sink, resulting in a segregated, fuel-rich region beneath the visible flame [5,6], with much lower local CE, e.g., Fig. 7 (b). Emissions from the stripped, unheated hydrocarbons are much harder to detect than partially combusted plumes using MWIR imagers, particularly in the presence of hot gases, due to the limited dynamic range of the instrument.

This detection issue is illustrated by Fig. 13. The lower part of the figure superimposes the CH_4 column density and isotherms at the centerline, while CH_4 mass flux ($kg \cdot m^{-1}s^{-1}$) and centerline temperature profiles for three sample transects are plotted at the top. A significant portion of the

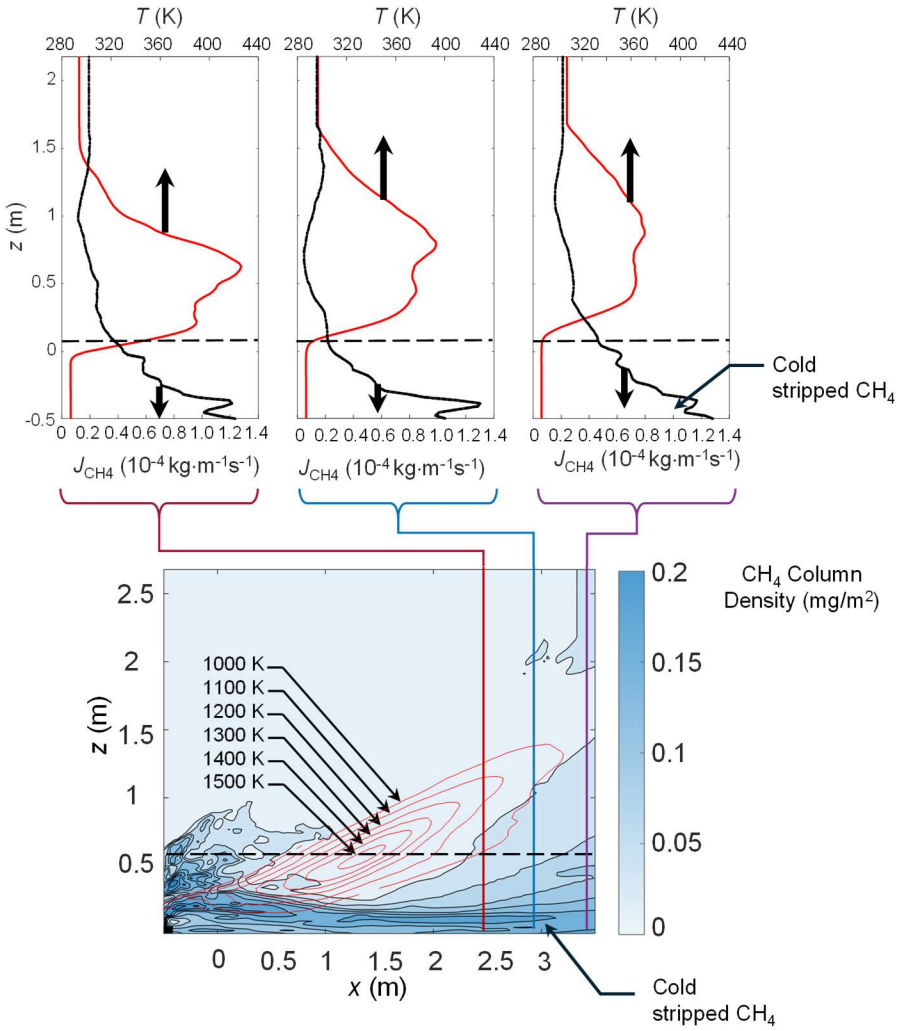

Fig. 13: Maps of CH_4 mass fluxes and centerline temperature contours at three cross-sections, along with the isotherms and column densities of CH_4 for an arbitrary timestep of Case 1. The fuel-rich region beneath the flare plume is unlikely to be detected using MWIR imaging, due to the limited dynamic range of the instrument.

unburned CH_4 leaving the computational domain through the downwind face comes from the stripping mechanism. Most of this CH_4 stream exists outside the VISR ROI and at temperatures that would be very difficult to detect using MWIR sensors.

Table *2* summarizes the fraction of methane that could potentially be detected by the VISR mechanism for the four scenarios considered here, indicating that a considerable amount of the CH_4 emissions from the flare would be unaccounted for using the VISR method. It is important to note that this is not a shortcoming of the VISR technique per se, but a limitation common to all remote sensing technologies based on MWIR imaging.

Table 2: Estimated capability of VISR to detect stripped (cold) CH_4. The third and fourth columns report the overall proportion of the fugitive methane comprised of cold methane, due to the aerodynamic-stripping mechanism, and the portion of stripped (cold) methane detectable by the VISR MWIR imager, respectively. The amount of cold methane is calculated by tracking the methane mass flux through multiple vertical transects, and identifying the region that remains below 100°C, the temperature at which steam and methane are introduced at the stack. The fraction of methane that can be imaged is estimated from the methane mass flux corresponding to pixels having a broadband intensity greater than the cutoff signal-to-noise ratio.

CFD-LES case ID	Stripped methane mass flow rate (g/s)	Contribution of stripped methane to the overall unburned methane	Proportion of stripped methane that can be imaged by the VISR instrument	Ground truth (CFD-driven) flare global CE
1	4.4	32 %	20 %	83.00 %
2	1.4	25 %	22 %	95.41 %
3	2.8	46 %	15 %	67.11%
4	2.5	37 %	12 %	61.48 %

6. CONCLUSIONS

Growing awareness of the environmental and health impacts of flare emissions motivates a need for technology that can measure flare combustion efficiency (CE) or destruction removal efficiency (DRE). While current state-of-the-art techniques like passive Fourier transform infrared spectroscopy (PFTIR) are confined to a single line-of-sight through the plume, the advent of commercial, high-speed mid-wavelength infrared imagers offers new opportunities for measuring CE in a manner that accounts for flare plume heterogeneity.

This paper examines the performance of a simplified version of video imaging spectro-radiometry (VISR), the first dedicated imager to be commercialized for flare emissions monitoring. While previous studies have assessed this technique by comparing VISR-derived CE/DRE values with those found using extractive sampling, we instead use a CFD-LES derived simulation as a "ground truth", which offers further insights into the validity of the simplifications and assumptions that underlie this approach and is also free of experimental artifacts associated with extractive plume sampling.

The analysis supports the simplifications made to the radiative transfer equation needed to derive a pixel-wise "local" CE, specifically the assumptions of an optically thin plume and a uniform temperature distribution along each pixel line-of-sight, although the latter assumption does not apply outside of the VISR region-of-interest, where there are expected to be strong gradients in temperature and species concentrations. On the other hand, the averaging technique

used to convert the local CE to global CE lacks a physical basis and produces biased estimates of the CE. Finally, our analysis highlights the important contribution of "stripped" fuel to the overall CE for flares, particularly under strong crosswind conditions. We find it unlikely that MWIR imaging approaches would be capable of imaging both the hot combustion gases and the unheated stripped fuel, suggesting that in these situations, VISR-derived CE values could overestimate the true CE by a considerable margin.

While we do not dispute that the technology can identify problematic operating conditions, e.g., due to steam over-assistance, our findings directly conflict with the manufacturer's claim of "accuracy within 1%". Given the impact of hydrocarbon emissions on climate change and pending regulations in multiple jurisdictions, the ability to quantify flare emissions and to understand the uncertainty attached to these estimates is critical. In our opinion, the VISR approach provides valuable insights into the operating characteristics of flares. However, we advocate a more nuanced and critical interpretation of the results, particularly given the limitations of the technology.

Data availability

The data used to carry out the analyses are openly available in "Viability of video imaging spectro-radiometry (VISR) for quantifying flare combustion efficiency," https://doi.org/4f19a082-58dc-4bcb-845c-991152673ea2.

Acknowledgements

This research was supported by the Natural Science and Engineering Research Council (NSERC RGPIN 2024 03824) and U.S. Department of Energy, Office of Science (DE-SC0017039). M.B. acknowledges the German Research Foundation (CRC129, 215035359) for supporting a research stay at the University of Waterloo.

References

[1] IPCC, "Climate Change 2021: The Physical Science Basis. Contribution of Working Group I to the Sixth Assessment Report of the Intergovernmental Panel on Climate Change," V. Masson-Delmotte, P. Zhai, A. Pirani, S. L. Connors, C. Péan, S. Berger, N. Caud, Y. Chen, L. Goldfarb, M. Gomis, M. Huang, K. Leitzell, E. Lonnoy, J. Matthews, T. Maycock, T. Waterfield, O. Yelekçi, R. Yu and B. Zhou, Eds., Cambridge UK, Cambridge University Press, 2021.

[2] J.H. Pohl, B.A. Tichenor, J. Lee, R. Payne, "Combustion efficiency of flares," *Combust. Sci. Technol.* 50, 217, 1986. (DOI: 10.1080/00102208608923934).

[3] World Bank. (2023). *Global Gas Flaring Tracker Report*. Retrieved from https://www.worldbank.org/en/programs/gasflaringreduction/global-gas-flaring-tracker

[4] G. Plant, E.A. Kort, A.R. Brandt, Y. Chen, G. Fordice, A.M. Gorchov Negron, S. Schwietzke, M. Smith, D. Zavala-Araiza, "Inefficient and unlit natural gas flares both emit large quantities of methane", *Science* 377 1566, 2022. (DOI: 10.1126/science.abq0385.)

[5] M. R. Johnson, D. J. Wilson, L. W. Kostiuk, "A fuel stripping mechanism for wake-stabilized jet diffusion flames in crossflow," *Combust. Sci. Technol.* 169, 155, 2001. (DOI: 10.1080/00102200108907844.)

[6] V.M. Torres, S. Herndon, Z. Kodesh, D.T. Allen, "Industrial flare performance at low flow concentrations. 1. Study overview." *Ind. Eng. Chem. Res.* 51, 12559, 2012. (DOI: 10.1021/ie202674t.)

[7] V.M. Torres, S. Herndon, D.T. Allen, "Industrial flare performance at low flow conditions. 2. steam- and air-assisted flares," *Ind. Eng. Chem. Res.* 51, 12569, 2012. (DOI: 10.1021/ie202675f.)

[8] A. Ahsan, H. Ahsan, J.S. Olfert, L.W. Kostiuk, "Quantifying the carbon conversion efficiency and emission indices of a lab-scale natural gas flare with internal coflows of air or steam," *Exp. Therm. Fluid. Sci.* 103, 133, 2019. (DOI: 10.1016/j.expthermflusci.2019.01.013.)

[9] M. Zamani, E. Abbasi-Atibeh, S. Mobaseri, H. Ahsan, A. Ahsan, J.S. Olfert, L.W. Kostiuk, "An experimental study on the carbon conversion efficiency and emission indices of air and steam co-flow diffusion jet flames," *Fuel* 287, 119534, 2021. (DOI: 10.1016/j.fuel.2020.119534.)

[10] M.R. Johnson, L.W. Kostiuk, "Efficiencies of low-momentum jet diffusion flames in crosswinds," *Combust. Flame* 123, 189, 2000. (DOI: 10.1016/S0010-2180(00)00151-6.)

[11] D.T. Allen, D. Smith, V.M. Torres, F.C. Saldaña, "Carbon dioxide, methane and black carbon emissions from upstream oil and gas flaring in the United States," *Curr. Opin. Chem. Eng.* 13, 119. 2016. (DOI: 10.1016/j.coche.2016.08.014.)

[12] World Bank. (2015). *Zero Routine Flaring by 2030.* Retrieved from https://www.worldbank.org/en/programs/zero-routine-flaring-by-2030.

[13] Government of Canada. (2023). *Regulations Amending the Regulations Respecting Reduction in the Release of Methane and Certain Volatile Organic Compounds (Upstream Oil and Gas Sector)*. *Canada Gazette, Part I*, 157(50). Retrieved from https://canadagazette.gc.ca.

[14] J. Wormhoudt, S.C. Herndon, J. Franklin, E.C. Wood, B. Knighton, S. Evans, C. Laush, M. Sloss, R. Spellicy, "Comparison of remote sensing and extractive sampling measurements of flare combustion efficiency," *Ind. Eng. Chem. Res.* 51, 12621, 2012. (DOI: 10.1021/ie202783m).

[15] T.R. Blackwood, "An evaluation of flare combustion efficiency using open-path Fourier Transform Infrared Technology," *J. Air Waste Manage. Assoc.* 50, 1714, 2000. (DOI: 10.1080/10473289.2000.10464206.)

[16] R. Haus, R. Wilkinson, J. Heland, K. Schäfer, "Remote sensing of gas emissions on natural gas flares," *Pure Appl. Opt.* 7, 853, 1998. (DOI: 10.1088/0963-9659/7/4/020.)

[17] R. Spellicy, M. Persky, 1984, *Flare efficiency monitoring by remote infrared sensing* (EPA Report No. 600/S7-84-053). U.S. Environmental Protection Agency.

[18] Clean Air Engineering, 2020, *PFTR flare testing: technology and method summary*. Retrieved from https://www.cleanair.com/resource/pftir-flare-testing-guide-technology-and-method-summary/?srsltid=AfmBOoooHU3VmYhpMGV7Ao-_our9JHGKU64P3TkglnAb05vq-VdVkMx5.

[19] S. Savary, J.-P. Gagnon, K. Gross, P. Tremblay, M. Chamberland, V. Farley, Standoff identification and quantification of flare emissions using infrared hyperspectral imaging, in: T. Vo-Dinh, R.A. Lieberman, G. Gauglitz (Eds.), Advanced Environmental, Chemical, and Biological Sensing Technologies VIII, SPIE, 2011: p. 80240T. https://doi.org/10.1117/12.884342.

[20] P. Lapeyre, R.B. Miguel, M.C. Nagorski, J.-P. Gagnon, M. Chamberland, C. Turcotte, K.J. Daun, "Quantifying flare combustion efficiency using an imaging Fourier transform spectrometer," *J. Air Waste Manage. Assoc.* 74, 319, 2024. (DOI: 10.1080/10962247.2024.2319773.)

[21] P. Lapeyre, N. S. Narayanan, M. Larivière-Bastien, K. J. Daun, "Quantifying flare combustion efficiency using a long wave infrared Fourier transform spectrometer," *Proc. Comb. Inst.* 40, 10554, 2024. (DOI: 10.1016/j.jqsrt.2024.109022.)

[22] Y. Zeng, J. Morris, M. Dombrowski (2012). *Multi-spectral infrared imaging system for flare combustion efficiency monitoring* (US Patent No. 9258495 B2). US Patent and Trademark Office.

[23] Y. Zeng, J. Morris, M. Dombrowski, "Validation of a new method for measuring and continuously monitoring the efficiency of industrial flares," *J. Air Waste Manag. Assoc*. 66, 76, 2015 (DOI: 10.1080/10962247.2015.1114045.)

[24] P. Tremblay, K.C. Gross, V. Farley, M. Chamberland, A. Villemaire, G.P. Perram, "Understanding and overcoming scene-change artifacts in imaging Fourier-transform spectroscopy of turbulent jet engine exhaust", in: S.S. Shen, P.E. Lewis (Eds.), *Imaging Spectrometry XIV*, SPIE, 2009: p. 74570F. (DOI: 10.1117/12.828001.)

[25] J.L. Harley, K.C. Gross, Remote quantification of smokestack effluent mass flow rates using imaging Fourier transform spectrometry, in: *Chemical, Biological, Radiological, Nuclear, and Explosives (CBRNE) Sensing XII*, 2011: p. 801813. (DOI: 10.1117/12.883193.)

[26] Providence Photonics LLC, *Flare Monitoring Continuous Flare Monitoring with Mantis™*. https://www.providencephotonics.com/flare-monitoring (accessed July 31, 2024).

[27] D.J. Corbin, M.R. Johnson, "Detailed Expressions and Methodologies for Measuring Flare Combustion Efficiency, Species Emission Rates, and Associated Uncertainties," *Ind. Eng. Chem. Res*. 53, 19359, 2014. (DOI: 10.1021/ie502914k.)

[28] I.E. Gordon, L.S. Rothman, R.J. Hargreaves, R. Hashemi, E.V. Karlovets, F.M. Skinner, E.K. Conway, C. Hill, R.V. Kochanov, Y. Tan, P. Wcisło, A.A. Finenko, K. Nelson, P.F. Bernath, M. Birk, V. Boudon, A. Campargue, K.V. Chance, A. Coustenis, B.J. Drouin, J. –M. Flaud, R.R. Gamache, J.T. Hodges, D. Jacquemart, E.J. Mlawer, A.V. Nikitin, V.I. Perevalov, M. Rotger, J. Tennyson, G.C. Toon, H. Tran, V.G. Tyuterev, E.M. Adkins, A. Baker, A. Barbe, E. Canè, A.G. Császár, A. Dudaryonok, O. Egorov, A.J. Fleisher, H. Fleurbaey, A. Foltynowicz, T. Furtenbacher, J.J. Harrison, J. –M. Hartmann, V. –M. Horneman, X. Huang, T. Karman, J. Karns, S. Kassi, I. Kleiner, V. Kofman, F. Kwabia–Tchana, N.N. Lavrentieva, T.J. Lee, D.A. Long, A.A. Lukashevskaya, O.M. Lyulin, V.Yu. Makhnev, W. Matt, S.T. Massie, M. Melosso, S.N. Mikhailenko, D. Mondelain, H.S.P. Müller, O.V. Naumenko, A. Perrin, O.L. Polyansky, E. Raddaoui, P.L. Raston, Z.D. Reed, M. Rey, C. Richard, R. Tóbiás, I. Sadiek, D.W. Schwenke, E. Starikova, K. Sung, F. Tamassia, S.A. Tashkun, J. Vander Auwera, I.A. Vasilenko, A.A. Vigasin, G.L. Villanueva, B. Vispoel, G. Wagner, A. Yachmenev, S.N. Yurchenko, "The HITRAN2020 molecular spectroscopic database," J. Quant. Spectrosc. Radiat. Transf., 277, 107949. 2022. (DOI: 10.1016/j.jqsrt.2021.107949.)

[29] A. Jatale, P.J. Smith, J.N., Thornock, S.T. Smith, M. Hradisky, "A validation of flare combustion efficiency predictions from large eddy simulations," *ASME J. Verif. Valid. Uncert. Quantif.* 1, 21001, 2016. (DOI: 10.1115/1.4031141.)

[30] J. Keck, D. Gillespie, "Rate-controlled partial-equilibrium methods for treating reacting gas mixtures," *Comb. Flame.* 17, 237, 1971. (DOI: 10.1016/S0010-2180(71)80166-9.)

[31] M. Janbozorgi, S. Ugarte, H. Metghalchi, J. C. Keck, "Combustion modeling of mono-carbon fuels using the rate-controlled constrained equilibrium method," *Comb. Flame*. 156, 1871, 2009. (DOI: 10.1016/j.combustflame.2009.05.013.)

[32] C.K. Westbrook, F.L. Dryer, "Simplified reaction mechanisms for the oxidation of hydrocarbon fuels in flames," *Comb. Sci. Technol.* 27, 31, 1981. (DOI: 10.1080/00102208108946970.)

[33] F.L. Dryer, I. Glassman, "High-temperature oxidation of CO and CH4," *Proc. Comb. Symp.*, 14 987, 1973. (DOI: 10.1016/S0082-0784(73)80090-6.)

[34] M.F. Modest, S. Mazumder, *Radiative Heat Transfer* (4th Ed.) Academic Press, 2022: pp. 563–616.